arXiv:1610.06137v2 [physics.plasm-ph] 31 Oct 2016

Langmuir wave filamentation in the kinetic regime. I. Transverse instability of Bernstein-Greene-Kruskal modes and multidimensional Vlasov simulations

Denis A. Silantyev,[1] Pavel M. Lushnikov,[1,*] and Harvey A. Rose[2,3]

[1] *Department on Mathematics and Statistics, University of New Mexico, New Mexico 87131, USA*
[2] *Theoretical Division, Los Alamos National Laboratory, MS-B213, Los Alamos, New Mexico, 87545*
[3] *New Mexico Consortium, Los Alamos, New Mexico 87544, USA*

(Dated: November 1, 2016)

Nonlinear Langmuir wave in the kinetic regime $k\lambda_D \gtrsim 0.2$ has a transverse instability, where k is the wavenumber and λ_D is the Debye length. The nonlinear stage of that instability develops into the filamentation of Langmuir waves which in turn leads to the saturation of the stimulated Raman scattering in laser-plasma interaction experiments. Here we study the linear stage of the transverse instability of the particular family [1] of Bernstein-Greene-Kruskal (BGK) modes [2] that is a bifurcation of the linear Langmuir wave. Performing direct $2+2D$ Vlasov-Poisson simulations of collisionless plasma we find the growth rates of oblique modes of the electric field as a function of BGK's amplitude, wavenumber and the angle of the oblique mode's wavevector relative to the BGK's wavevector. Results of the simulations are compared to the theoretical predictions.

I. INTRODUCTION

Consider a Langmuir wave [3] (LW) wave packet with a typical wavenumber k. If $k\lambda_D \ll 1$, then the hydrodynamic approximation (the "fluid" regime) [4, 5] of LW is valid, where λ_D is the Debye length. In that regime a three dimensional ($3D$) catastrophic collapse [3] may occur: the LW's ponderomotive force causes a localized plasma density depression, δn, proportional to the squared LW electric field amplitude E, i.e. $\delta n \sim -|E|^2$. It results in downshifting LW's frequency and [6–8] trapping the LW. That trapping in turn causes the growth of $|E|$, larger δn and so on until catastrophic LW collapse occurs. As shown in Ref. [9], the transition from the fluid to the "kinetic" regime occurs at $k\lambda_D \sim 0.2$ when the trapped electron effects, such as frequency shift cannot be ignored. Thus at $k\lambda_D \gtrsim 0.2$, LW frequency reduction due to electron trapping may dominate [9] the ponderomotive [5] shift. Though the trapped electron frequency shift, perturbatively, varies as $|E|^{1/2}$, and therefore cannot lead to LW collapse, $3D$ particle-in-cell (PIC [10]) simulation results have been interpreted as showing that the trapped electron LW filamentation instability can saturate [11] stimulated Raman back-scatter (SRS) [12] by reducing the LWs coherence. In actual plasma, the SRS daughter LW is subject to other instabilities, such as LW-ion-acoustic decay (LDI). Fluid and kinetic regime LDI have been observed in SRS simulations [11, 13] while kinetic regime LDI has been experimentally [14] noted [15].

Additional complexity in the interpretation of experimental data gathered from laser-plasma interaction arises from instabilities of the laser beam [16] coupled [17–19] to relatively low frequency ion-acoustic waves. Since direct experimental data pointing to kinetic LW filamentation has not been available, first principles simulation of pure LW dynamics is perhaps the cleanest way to "see" this phenomenon. Fully nonlinear PIC simulations [20] with Bernstein-Greene-Kruskal (BGK) mode [2] initial conditions have shown qualitative agreement with LW filamentation theory [9, 21], but the theory's finer points, such as instability thresholds, require a noise free model, namely the Vlasov simulations.

Here we address the LW filamentation in the kinetic regime $k\lambda_D \gtrsim 0.2$ by studying the transverse instability of BGK modes using $2+2D$ fully spectral Vlasov simulations. BGK modes are constructed following the approach of Ref. [1] to approximate the adiabatically slow pumping by SRS. We concentrate on the linear stage of the transverse instability development while observing strong LW filamentation in the nonlinear stage. Also in the second paper (Part II) of the series we consider dynamically prepared BGK-like initial conditions created with the adiabatically slow SRS-like pumping and study the transverse instability of those waves comparing with the results for BGK modes in this paper.

The paper is organized as follows. Section II introduces Vlasov-Poisson equation and the general BGK modes (equilibrium states). In Section III A we recall a special family [1] of $1+1D$ BGK modes that bifurcates form linear LW. We describe the procedure of analytical and numerical construction of these modes. Section III B outlines their nonlinear dispersion relation and Section III C provides the analytical results on the growth rate of transverse instability of these BGK modes. In Section IV we provide results of numerical $2+2D$ Vlasov simulations. Section IV A is devoted to the settings of our Vlasov simulations and the numerical methods used. Section IV B addresses transverse instability results and their comparison with the theory. Section IV C provides a comparison of the growth rates obtained in Section IV B with the growth rates from PIC code simulations of Ref. [20]. In Section V the main results of the paper are discussed.

* plushnik@math.unm.edu

II. BASIC EQUATIONS

The Vlasov equation for the phase space distribution function $f(\mathbf{r}, \mathbf{v}, t)$, in units such that electron mass m_e and charge e are normalized to unity, the spatial coordinate $\mathbf{r} = (x, y, z)$ to the electron Debye length λ_D, the time t to reciprocal electron plasma frequency, $1/\omega_{pe}$, [22] and the velocity $\mathbf{v} = (v_x, v_y, v_z)$ is normalized to the the electron thermal speed v_e, is

$$\left\{ \frac{\partial}{\partial t} + \mathbf{v} \cdot \nabla + \mathbf{E} \cdot \frac{\partial}{\partial \mathbf{v}} \right\} f = 0, \tag{1}$$

where $\mathbf{E}$ is the electric field scaled to $k_B T_e/(\lambda_D e)$. Here T_e is the background electron temperature and k_B is the Boltzmann constant. Magnetic field effects are ignored for clarity. Then in the electrostatic regime

$$\mathbf{E} = -\nabla \Phi, \tag{2}$$

with the electrostatic potential Φ given by Poisson's equation

$$\nabla^2 \Phi = -\rho, \tag{3}$$

where the electron density ρ is given by

$$\rho(\mathbf{r}, t) = \int f(\mathbf{r}, \mathbf{v}, t) d\mathbf{v} \tag{4}$$

and the factor 4π is absent in equation (3) because of the chosen normalization.

Equations (1)-(4) form a closed Vlasov-Poisson system. Finite amplitude travelling wave solutions of that system such that they correspond to steady state solutions in the reference frame moving with a phase velocity v_φ are called by Bernstein-Greene-Kruskal (BGK) modes [2]. Here we assume without loss of generality that z is chosen in the direction of v_φ so that the time dependence of f is given by $f(\mathbf{r}_\perp, z - v_\varphi t, \mathbf{v})$, $\mathbf{r}_\perp \equiv (x, y)$. Then equation (1) is reduced to

$$(v_z - v_\varphi) \frac{\partial}{\partial z} f + \mathbf{v}_\perp \cdot \nabla f + \mathbf{E} \cdot \frac{\partial}{\partial \mathbf{v}} f = 0. \tag{5}$$

General solution of equations (2) and (5) is given by $f = g\,(W)$, where g is the arbitrary function of the single scalar argument

$$W \equiv \frac{(v_z - v_\varphi)^2}{2} + \frac{\mathbf{v}_\perp^2}{2} + \Phi(\mathbf{r}_\perp, z - v_\varphi t) \tag{6}$$

which is the single particle energy (the sum of the kinetic energy in the moving reference frame and the electrostatic energy).

BGK modes are obtained if we require $g(W)$ to satisfy equations (3) and (4) [2]. That requirement still leaves a significant freedom to construct different types of BGK modes (time independent solutions in the moving frame).

III. BGK MODE LINEAR FILAMENTATION INSTABILITY

Our goal is to study the transverse stability of BGK modes. In general, a linear instability is specific to a given BGK mode. We intend to choose BGK mode that is dynamically selected (at least approximately) by SRS with z being the direction of laser beam propagation in plasma. The simplest BGK family has a nontrivial solution f_{BGK} in $1 + 1D$ (one space and one velocity dimension [2]) with no dependence on the transverse coordinate $\mathbf{r}_\perp$, while the dependence on the transverse velocity $\mathbf{v}_\perp$ being trivially Maxwellian as follows

$$f = f_{BGK}(z - v_\varphi t, v_z) \frac{\exp(-\mathbf{v}_\perp^2/2)}{2\pi}. \tag{7}$$

Our initial model [1] of the SRS daughter LW in a laser speckle is presented in Eq. (12) below. If a time-dependent Vlasov equation solution has a symmetry, e.g., in $2 + 2D$ (two space and two velocity dimensions) when the initial condition (and possible external potential) only depend on one spatial coordinate z, or in $3 + 3D$ a cylindrically symmetric configuration, then an instability may break that symmetry, allowing for a determination of growth rate. The former, revisited here, was explored in $2 + 2D$ Vlasov simulations [23], while the latter was observed [11] in $3D$ PIC, SRS single speckle simulations. In addition, we present LW filamentation (transverse instability) growth rates of linear fluctuations about a particular class of BGK modes, recalled in the next Section III A.

A. Construction of 1+1D BGK

The beating of laser and SRS light provides a source of LWs thus pumping BGK modes. Following Ref. [1], we assume that the laser intensity is just above SRS instability threshold. Then the pumping of LWs is slow and can be idealized as a travelling wave sinusoidal external potential Φ_{ext}, with the amplitude ϕ_{pump}, the phase speed v_φ and the wavenumber k_z such that

$$\Phi_{ext} = \phi_{pump} \cos[k_z(z - v_\varphi t)],\ k_z = |\mathbf{k}|. \tag{8}$$

The total electrostatic potential, Φ, is given by

$$\Phi = \Phi_{ext} + \Phi_{int}, \tag{9}$$

where the internal potential Φ_{int} is determined from Poisson's equation (10), where $f_{1D}(z, v_z, t)$ is the $1D$ electron phase space distribution function.

$$-\frac{\partial^2 \Phi_{int}}{\partial z^2} = \int f_{1D} dv_z, \tag{10}$$

Inertial confinement fusion applications require a beam smoothing [24–26] resulting in the laser intensity, to form a time-dependent speckle field. The external pumping is

at maximum in a laser speckle which is a local maximum of laser beam intensity. Intense speckles have a width approximately $F\lambda_0$, with F the optic f-number (the ratio of the focal length of the lens divided by the lens diameter) and λ_0 the laser wavelength. The temporal scale t_c of beam smoothing is typically large compare with the inverse growth rate $1/\gamma_{SRS}$ of SRS (e.g. for the National Ignition Facility [25, 26] $t_c \sim 4$ps and typically $1/\gamma_{SRS} \sim 0.03$ps). It implies that the speckle can be considered as time-independent which we assume below. Electrons, with the typical speed v_e, cross a speckles width in a dimensional time scale $1/\nu_{SideLoss} \propto F\lambda_0/v_e$, where c is the speed of light, n_e and n_c are the average and critical electron densities, respectively. As a result, f_{1D} tends to relax to the background distribution function, f_0, assumed Maxwellian,

$$f_0(v_z) = \frac{\exp(-v_z^2/2)}{\sqrt{2\pi}} \tag{11}$$

at the rate $\nu_{SideLoss}$. These considerations motivate our $1+1D$ model of BGK generation by introducing the relaxation term $-\nu_{SideLoss}[f_{1D}(z,v_z,t) - f_0(v_z)]$ into the Vlasov equation (1) as follows. In the wave frame (switching to that frame implies $z \to z + v_\varphi t$ and $v_z \to v_z + v_\varphi$),

$$\begin{aligned} &\left\{ \frac{\partial}{\partial t} + v_z \frac{\partial}{\partial z} - \frac{\partial \Phi}{\partial z}\frac{\partial}{\partial v_z} \right\} f_{1D}(z,v_z,t) = \\ &- \nu_{SideLoss}[f_{1D}(z,v_z,t) - f_0(v_z+v_\varphi)]. \end{aligned} \tag{12}$$

Let f_{eq} be a time independent solution of Eq. (12). In the double limit

$$f_{BGK} = \lim_{\phi_{pump}\to 0} \lim_{\nu_{SideLoss}\to 0} f_{eq}, \tag{13}$$

a particular BGK mode which bifurcates [27, 28] from a linear LW, f_{BGK}, may be obtained [1]. This mode correspond to the adiabatically slow pumping by SRS. It depends on (z, v_z) only through the single particle energy, W,

$$W = \Phi(z) + v_z^2/2 \tag{14}$$

which is the restriction of equation (6) to 1+1D case in the wave frame with $\Phi(\mathbf{r}_\perp, z - v_\varphi t) \to \Phi(z)$.

There are two methods to construct BGK modes in question. First method is numerical one and implies that we numerically solve equations (8)-(12) for each values of ϕ_{pump} and $\nu_{SideLoss}$ followed by taking numerically the double limit (13). Second method is analytical one and is based on the integration along the particle orbits of the time independent solution of Eq. (12), where the double limit (13) is evaluated analytically. We investigated both methods, found that they give similar results, but choose below to focus on the second method only since it is a simpler to implement and free of numerical issues.

The electrostatic potential Φ traps electrons with velocities close enough to v_φ such that they cannot go over barriers created by Φ. Thus for different electrons there are both passing orbits outside the trapping region and periodic orbits inside the trapping region. Recall that passing orbits can have either positive or negative velocities, and this must be specified along with W. It was shown in Refs. [29] and [1] that taking the double limit (13) in the equation Eq. (12) we get

$$f_{BGK}(W) = \oint_W f_0[v(s) + v_\varphi] ds / T(W). \tag{15}$$

The integral sign here denotes integration around a particular orbit with constant W. The time-like characteristic variable s, used in integration, parametrizes a particular orbital location $(z(s), v(s))$ through the characteristic equations

$$dz/ds = v,\ dv/ds = -d\Phi/dz. \tag{16}$$

Also $T(W)$ denotes the orbit's period,

$$T(W) = \oint_W ds. \tag{17}$$

Here and throughout the remaining part of Section III we replace v_z by $v(.)$ when it describes the velocity of a particular electron with energy W as a function of some parameter (s or z), while we think of v_z as independent variable in the rest of the formulas. Also we abuse notation and use the same symbols for v and f_{BGK} irrespective of their parametrization by different variables. Φ is assumed periodic so that all orbits are closed by periodicity (including the passing orbits).

Assume $\Phi(z)$ is the given function of z. Then using Eq. (14), changing the integration variable from s to z in Eqs. (15) and (17), we can express $T(W)$ and $f_{BGK}(W) \equiv f_{BGK}(z, v_z)$ at any point (z, v_z) in the phase space as follows (see also Fig. 1 for the addition insight)

$$T(W) = \begin{cases} 4\int_0^{z_{max}} \frac{dz}{v(z)},\ \Phi_{min} < W < \Phi_{max}, \\ \int_0^{L_z} \frac{dz}{v(z)},\ W > \Phi_{max}, \end{cases} \tag{18}$$

$$\Phi_{min} \equiv \min_z \Phi(z),\ \Phi_{max} \equiv \max_z \Phi(z),\ L_z \equiv \frac{2\pi}{k_z}$$

and

$$f_{BGK}(W) =$$

$$\begin{cases} 2\int_0^{z_{max}} \frac{f_0[v_\varphi + v(z)] + f_0[v_\varphi - v(z)]dz}{v(z)},\ \Phi_{min} < W < \Phi_{max}, \\ f_0(v_\varphi),\ W = \Phi_{max}, \\ \int_0^{L_z} \frac{f_0[v_\varphi + v(z)]dz}{v(z)},\ W > \Phi_{max} \text{ and } v_z > v_\varphi, \\ \int_0^{L_z} \frac{f_0[v_\varphi - v(z)]dz}{v(z)},\ W > \Phi_{max} \text{ and } v_z < v_\varphi, \end{cases} \tag{19}$$

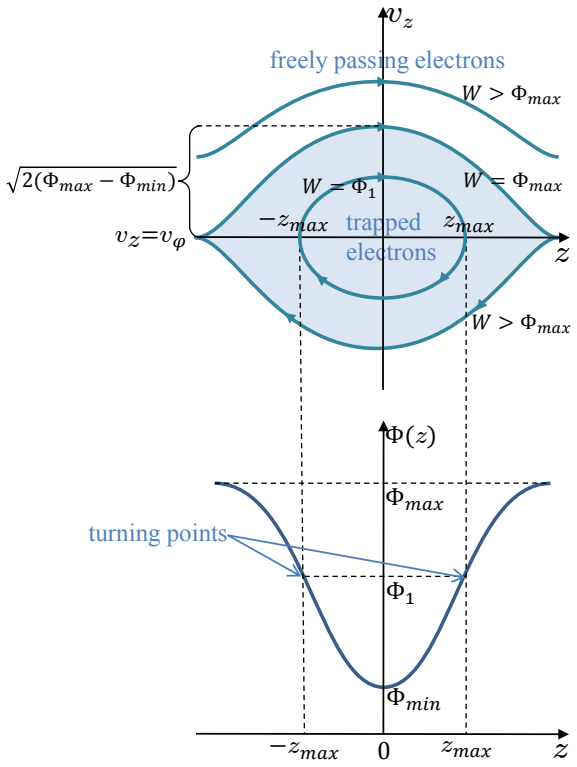

FIG. 1. Schematics of the electric potential and the corresponding trapping region of $f_{BGK}(z, v_z)$.

where $v(z)$ is determined from Eq. (14) as

$$v(z) = \sqrt{2[W - \Phi(z)]} \tag{20}$$

and we assume that $\Phi(z)$ has a single local maximum and a single local minimum per period L_z. Also z_{max} is obtained by numerically inverting $\Phi(z_{max}) = W$ (see Fig. 1 for the illustration). Note that it is also possible to integrate Eqs. (15) and (17) directly in s variable which has more compact form compared to Eqs. (18) -(19). However, we chose to use Eqs. (18)-(20) because it is easier to implement a high-order numerical scheme for integrals (18) and (19) that depend only on one independent variable rather than calculating integrals in Eqs. (15)-(17) that require two-step process, first numerically finding particle's orbit $(z(s), v(s))$ and then computing the integrals.

The amplitudes of Fourier harmonics of $\Phi(z)$ are rapidly decaying [1], so we start by constructing a BGK mode approximately by taking into account only the first harmonic

$$\Phi(z) = -\phi_0 \cos(k_z z) \tag{21}$$

parametrized by the amplitude ϕ_0. Then the comparison with definitions in Eq. (18) imply that $\Phi_{min} = -\phi_0$, $\Phi_{max} = \phi_0$, $v(z) = \sqrt{2(W + \phi_0 \cos(k_z z))}$ and $z_{max} = \frac{1}{k_z} \arccos(\frac{-W}{\phi_0})$.

Integrating f_{BGK} over v_z that was obtained from Eqs. (18)-(20) and using the Poisson's equation (10), we get

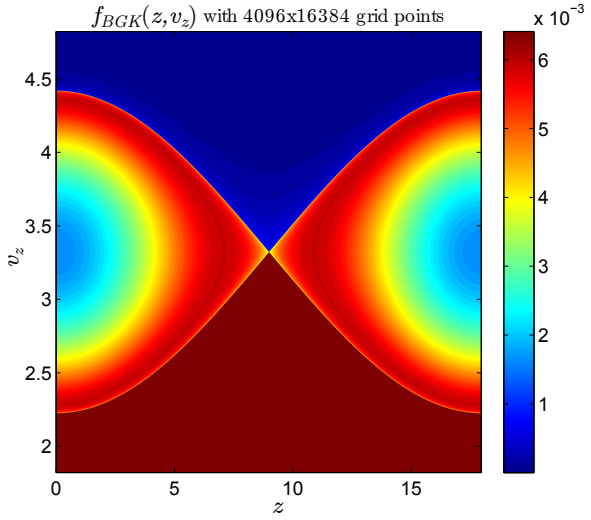

FIG. 2. The phase space density distribution function $f_{BGK}(z, v_z)$ of BGK mode with $k_z = 0.35, \phi_0 = 0.3, v_\varphi = 3.321836\ldots$.

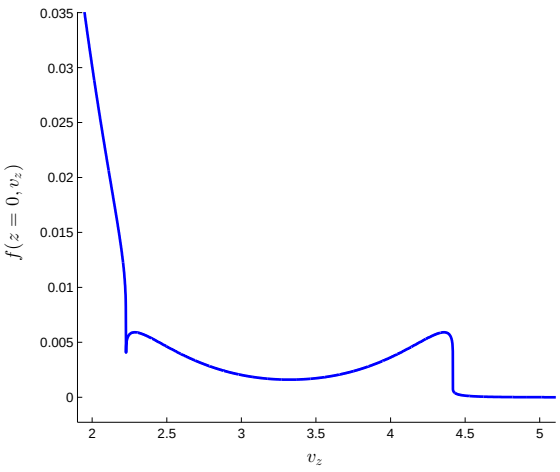

FIG. 3. Cross-section of $f_{BGK}(z = 0, v_z)$ for BGK mode with $k_z = 0.35, \phi_0 = 0.3, v_\varphi = 3.321836\ldots$.

the corresponding electrostatic potential $\Phi_{approx}(z)$ of the approximate BGK solution. One can use k_z as the free parameter to rescale the solution in such a way that the amplitude of the first harmonic in the electrostatic potential is equal to ϕ_0 as was assumed in Eq. (21).

The found solution is however indeed only approximate because generally it is not self-consistent due to presence of higher order Fourier harmonics beyond assumed $\Phi(z)$ in Eq. (21). Our calculations show that the second harmonic is typically 2-3 orders of magnitude less compared to the first one even for ϕ_0 of order 1, which validates our initial assumption. We found it satisfactory for the purpose of the subsequent results of this paper to stop the process of BGK construction at this point. However we also used $\Phi_{approx}(z)$ to obtain the corresponding updated $f_{BGK}(z, v_z)$ from Eqs. (18)-(20), calculated second iter-

ation of $\Phi_{approx}(z)$, and so on. We found that typically ~ 20 iterations is sufficient to converge $\Phi_{approx}(z)$ within 10^{-15} relative pointwise error over z (with the relative error being $\sim 1\%$ after first iteration) to the exact BGK mode. In this way one can construct a BGK mode for given values of ϕ_0 and v_φ as the input parameters producing the values of k_z as the output parameter together with f_{BGK}. If one needs to find f_{BGK} with the specified value of $k_z = k_{z,input}$ then Newton iterations are performed to find a root of $k_{z,input} - k_{z,output}(\phi_0, v_\varphi) = 0$ as a function of either ϕ_0 or v_φ keeping the other variable fixed. Here $k_{z,output}(\phi_0, v_\varphi)$ is the values of k_z obtained for given ϕ_0 and v_φ from the procedure described above.

An example of BGK mode constructed using this approach with Newton iterations over v_φ for $k_{z,input} = k_z = 0.35$, $\phi_0 = 0.3$ and resulting $v_\varphi = 3.321836\ldots$ is shown in Figs. 2-3. Fig. 2 shows $f_{BGK}(z, v_z)$ around the trapping region. It has a jump discontinuity along separatrix $\Phi(z) + v_z^2/2 = W = \Phi_{max}$. Fig. 3 shows the widest cross-section of the the trapping region at $z = 0$.

B. Trapped electron filamentation dispersion relation

LW filamentation dispersion relations have been presented in Refs. [9] and [23], but we believe that a more cogent and general result was obtained in Ref. [21], which we now review. Let x denote a direction perpendicular to the LW propagation direction, the z axis, with wave amplitude ϕ_{eq} , the maximum value, in equilibrium, of Φ over z (in particular case given by Eq. (21), $\phi_{eq} = \phi_0$). Unlike the linear regime, in which the parameters k_z and v_φ are related via well-known ϕ_{eq}-independent dispersion relations [30, 31], a BGK mode's dispersion relation is amplitude dependent. The BGK mode family identified by Eqs. (12) and (13), has a nonlinear dispersion relation determined [27, 28] by setting the real part of the dielectric function, ε, to zero. Recall that we define the nonlinear dielectric function ε as $\Phi = \Phi_{ext}/\varepsilon$ with Φ_{ext} being the external pump from SRS (8). To lowest order in $\sqrt{\phi_{eq}}$ using f_{BGK} given by Eqs. (18)-(21) one obtains [1] that,

$$0 = k_z^2 \mathrm{Re}[\varepsilon] \approx k_z^2 - \mathrm{Re}[\Xi_0(v_\varphi)] + 1.76 f_0''(v_\varphi)\sqrt{\phi_{eq}}, \quad (22)$$

where

$$\Xi_0(v) = Z'(v/\sqrt{2})/2,$$
$$Z(v) = e^{-v^2}\sqrt{\pi}(i - \mathrm{erfi}(v)) = e^{-v^2}(i\sqrt{\pi} - 2\int_0^v e^{t^2} dt)$$

and Z is the plasma dispersion function [32].

Eq. (22) can be solved for $\phi_{eq}(k_z, v_\varphi)$, solutions are illustrated by Fig. 4. For $k_z = 0.35$ the maximum value of $\phi_{eq} \approx 0.78$ is at $v_\varphi \approx 2.85$. The nonlinear LW dispersion relation corresponds to values of v_φ greater than the values found at the maxima. The electron acoustic [33] wave (EAW) dispersion relation corresponds to values of v_φ less than the values found at the maxima.

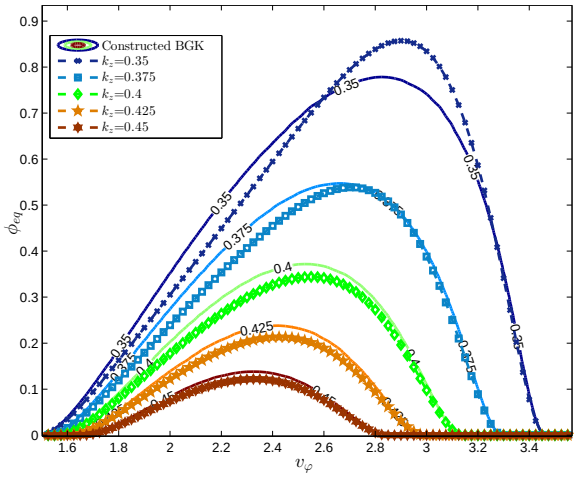

FIG. 4. LW and EAW potential amplitude versus phase velocity for various k_z. Solid lines represent constructed BGK family dispersion relation, dashed - approximation of dispersion relation by formula (22).

Alternatively, v_φ may be considered as a function of k_z and ϕ_{eq}, i.e. $v_\varphi(k_z, \phi_{eq})$, by inverting the graph shown in Fig. 4. Since a travelling waves angular frequency, ω, is always the product of wavenumber and phase velocity, $\omega = k_z v_\varphi$, one may re-express the nonlinear dispersion relation as a wavenumber and amplitude dependent ω,

$$\omega(k_z, \phi_{eq}) = k_z v_\varphi(k_z, \phi_{eq}). \quad (23)$$

as presented in Eqs. (48) and (49) of Ref. [1], and in Eq. (7) and Fig. [7] of Ref. [9].

C. Trapped electron filamentation transverse instability

We now consider the transverse instability of f_{BGK}. Near the equilibrium (BGK mode) in the moving frame, let

$$\Phi = \mathrm{Re}\left\{\exp(i\mathbf{k}\cdot\mathbf{r})[\phi_{eq} + \delta\phi(t)\exp(i\delta\mathbf{k}\cdot\mathbf{r})]\right\}, \quad (24)$$

where $\mathbf{k}$ is parallel to z direction and $\delta\mathbf{k}$ is responsible for the transverse perturbations with the amplitude $\delta\phi(t)$. Let $\delta\phi \sim exp(\gamma t)$. In Ref. [21] it was shown that

$$(\gamma + \nu_{residual})^2 = -D\left(\phi_{eq}\frac{\partial\omega}{\partial\phi_{eq}} + D\right), \quad (25)$$

wherein the generalized diffraction operator, D,

$$2D = \omega(|\mathbf{k} + \delta\mathbf{k}|, \phi_{eq}) + \omega(|\mathbf{k} - \delta\mathbf{k}|, \phi_{eq}) - 2\omega(|\mathbf{k}|, \phi_{eq}) \quad (26)$$

reduces to the diffraction coefficient, $(|\delta\mathbf{k}_\perp|^2/2|\mathbf{k}|)(\partial\omega/\partial|\mathbf{k}|) + (\delta k_z^2/2)\partial^2\omega/\partial|\mathbf{k}|^2$, for small $|\delta\mathbf{k}|$. When $\delta\mathbf{k}\cdot\mathbf{k} = 0$, Eq. (26) simplifies to

$$D = \omega(|\mathbf{k} + \delta\mathbf{k}|, \phi_{eq}) - \omega(|\mathbf{k}|, \phi_{eq}), \quad (27)$$

and the (possible) instability is customarily called filamentation, our main regime of interest.

Also assuming $\phi_{eq} \ll 1$ in addition to $\delta\mathbf{k}\cdot\mathbf{k}=0$ and $|\delta\mathbf{k}| \ll 1$, we can approximate Eq. (27) as follows

$$D \approx D_{lin} = \frac{1}{2k_z}\frac{\partial\omega(|\mathbf{k}|,0)}{\partial|\mathbf{k}|}\bigg|_{|\mathbf{k}|=k_z}|\delta\mathbf{k}|^2 = \frac{v_g}{2k_z}|\delta\mathbf{k}|^2, \quad v_g \equiv \partial\omega(|\mathbf{k}|,0)/\partial|\mathbf{k}|, \tag{28}$$

where v_g is the group velocity corresponding to the dispersion relation (22) and (23) for $\phi_{eq}=0$, $v_g = 1.0080$ for $k_z = 0.35$.

The residual damping, $\nu_{residual}$, from Eq. (25) is model dependent. For example, if the double limit of Eq. (13) stops short of zero value, but with

$$\frac{\nu_{residual}}{\omega_{bounce}} \ll 1, \quad \frac{\phi_{pump}}{\phi_{eq}} \ll 1, \quad \frac{\omega_{bounce}}{\omega_{pe}} = k_z\sqrt{\phi_{eq}}, \tag{29}$$

or in dimensional units, $\frac{\omega_{bounce}}{\omega_{pe}} = k_z\lambda_D\sqrt{e\phi_{eq}/k_BT_e}$. Then it follows from Eqs. (28), (71) of Ref. [1] and Fig. 3 of Ref. [1] that, for $v_\varphi \gtrsim 2.2$, in dimensional units,

$$\nu_{residual} \approx \frac{\omega_{pe}}{2}\mathrm{Im}[\varepsilon] \gtrsim \frac{\nu_{SideLoss}}{\omega_{bounce}}\nu_{Landau}. \tag{30}$$

In Eq. (30), the Landau damping rate, ν_{Landau}, is evaluated for a linear LW with wavenumber k_z. Also if $|\delta\mathbf{k}| \ll |\mathbf{k}|$ is not satisfied, it has been argued [23] that $\nu_{residual}$ is augmented by an amplitude dependent, but $\nu_{SideLoss}$ independent, form of Landau damping. However, as we discuss in Section IV B below, that addition to $\nu_{residual}$ is not consistent with our simulation results and we set $\nu_{residual}=0$ in (25) below.

Eq. (23) may be used to find $\partial\omega/\partial\phi_{eq}$ in terms of $\partial v_\varphi/\partial\phi_{eq}$ which in turn may be obtained by applying $\partial/\partial\phi_{eq}$ to Eq. (22).

$$\{Re[\Xi_0'(v_\varphi)] - 1.76f_0'''\sqrt{\phi_{eq}}\}\frac{\partial v_\varphi}{\partial\phi_{eq}} = \frac{1.76f_0''(v_\varphi)}{2\sqrt{\phi_{eq}}}. \tag{31}$$

In the kinetic regime, D may assume negative values as $|\delta\mathbf{k}|$ [9] and/or ϕ_{eq} [21] increase. Therefore, the qualitative shape of γ contours determined by Eqs. (22), (25) and (26) may differ from fluid model modulational/filamentation [23], whose domain of applicability is limited, a priori, to $k_z \ll 1$. Contours of γ for $k_z = 0.35$ are shown in Figs. 5, with $\nu_{residual}$ set to 0. For more contours of γ and related figures see [21]. If we use linear approximation for D as in Eq. (28) and solve Eqs. (22), (25) for $k_z = 0.35$ and $\nu_{residual}=0$ we get contours of γ as shown in Fig. 6.

Another simplification can be made if one assumes at the leading order that the nonlinear frequency shift $\Delta\omega \propto \sqrt{\phi_{eq}}$. Then $\phi_{eq}\frac{\partial\omega}{\partial\phi_{eq}} = \Delta\omega/2$ and maximizing γ over D in Eq. (25) we obtain the maximum value

$$\gamma^{max} = |\Delta\omega|/4, \tag{32}$$

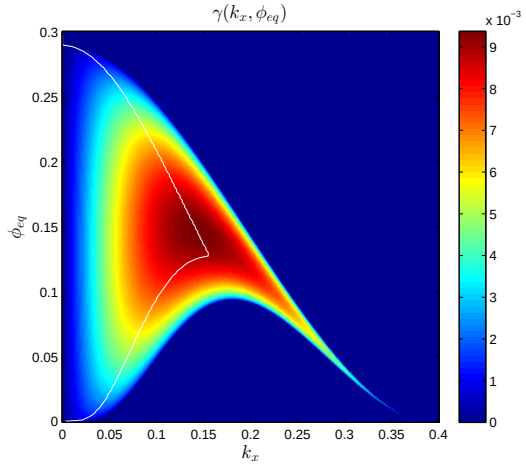

FIG. 5. LW filamentation growth rate contours for $k_z = 0.35$. White line shows the maximum growth rate for given ϕ_{eq}.

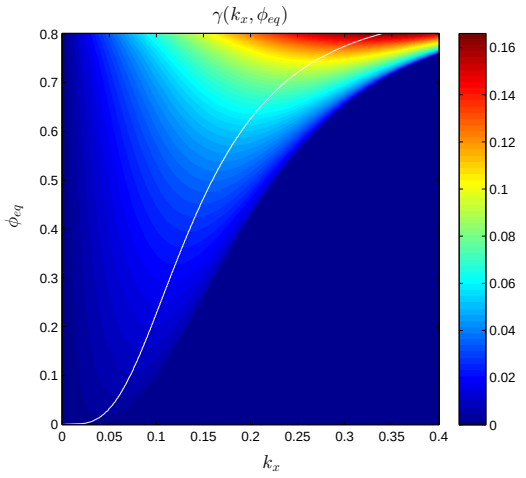

FIG. 6. LW filamentation growth rate contours for $k_z = 0.35$ using linear approximation for D as in (28). White line shows the maximum growth rate for given ϕ_{eq}.

at

$$D = -\Delta\omega/4, \tag{33}$$

which is valid for $|\delta\mathbf{k}| \ll |\mathbf{k}|$ and $\nu_{residual}=0$. Using the approximation (28), we obtain from Eq. (33) the position of the maximum

$$|\delta\mathbf{k}| = k_x^{max} = \left(\frac{-\Delta\omega\, k_z}{2v_g}\right)^{1/2}. \tag{34}$$

IV. NUMERICAL SIMULATIONS OF LW FILAMENTATION

Here we describe $2+2D$ fully non-linear Vlasov simulations that we performed to study the transverse instability of BGK modes described in the previous section.

A. Simulation settings and methods

We simulate $2+2D$ Vlasov-Poisson system (1)-(4) in the phase space (z, v_z, x, v_x) using fully spectral (in all four dimensions) code and split-step (operator splitting) method of 2nd order in time with periodic boundary conditions (BC) in all four dimensions. To ensure a spectral convergence and imitate the weak effect of collisions, we added to Eq. (1) a small additional hyper-viscosity term into Eq. (2) as follows

$$\left\{\frac{\partial}{\partial t}+v_z\frac{\partial}{\partial z}+v_x\frac{\partial}{\partial x}+E_z\frac{\partial}{\partial v_z}+E_x\frac{\partial}{\partial v_x}\right\}f= \\ -D_{16v_z}\frac{\partial^{16}}{\partial v_z^{16}}\left(f-\frac{1}{L_z}\int_0^{L_z}f dz\right), \tag{35}$$

where D_{16v_z} is the 16th order hyper-viscosity coefficient. We use periodic BC in z direction with the period $L_z=2\pi/k_z$ and $k_z=0.35$ in our simulations. Choosing $L_z=2\pi/k_z$ allows to focus on the study of transverse instability effects (along x) while avoid subharmonic (sideband instability) [34] in longitudinal z-direction. Periodic BC in x with the period L_x together with x-independent initial condition (IC) are used to separate transverse instability effects from any sideloss effects due to trapped electrons traveling in the transverse direction (this is in contrast to Ref. [35], where the transverse spatial profile in the initial condition made sideloss comparable with the transverse growth rate). We chose typically $200\pi \le L_x \le 800\pi$ depending on amplitude of BGK or EPW to capture all growing transverse modes. Periodic BC in v_z and v_x were used without sacrificing any accuracy of the simulation compared to outgoing BC since the particle flow through the boundary at $v_z=v_z^{max}$ is $\propto E_z\frac{\partial f}{\partial v_z}$ with $\frac{\partial f}{\partial v_z}\approx\frac{v_z}{\sqrt{2\pi}}e^{-\frac{v_z^2}{2}}$ which can be made as small as desired by picking large enough v_z^{max}. Typically we choose $v_z^{max}=8$ for which $|E_z\frac{\partial f}{\partial v_z}|\approx 10^{-15}$. The same argument is applied in v_x direction with the only difference that in our simulations E_x is several orders less than E_z so v_x^{max} can be chosen smaller than v_z^{max}. Typically we choose $v_x^{max}=6$ for which the flow through $v_x=v_x^{max}$ boundary is at the level of machine precision.

Split-step method of 2nd order was chosen over other methods since it is unconditionally stable (which allows large time steps), preserves number of particles at each time step exactly and has a very small error in the full energy of the system. That error is not accumulated in time (in contrast with Runge-Kutta methods their such accumulation occurs). We also decided to choose 2nd order method over higher orders methods because our experiments with the size of time step and methods of various orders showed that the time integration error is dominated by the errors coming from other sources (space discretization and hyper-viscosity term).

The hyper-viscosity term in the right-hand side (r.h.s.) of Eq. (35) is used to prevent recurrence [36] and aliasing (which causes propagation of numerical error from high modes to low modes) effects. The hyper-viscosity operator in r.h.s. of Eq. (35) has to be a smooth function in the Fourier transformed v_z space. At the same time we found beneficial to use high-order (here we choose 16th order) over low-order hyper-viscosity since it affects low modes of solution less while having effectively the same damping effect on high modes. That allows to use the smaller numerical grid for the same overall precision. The coefficient D_{16v_z} is chosen as small as possible to prevent aliasing depending on the resolution of simulation in v_z directions. Our safe estimate $D_{16v_z}\approx|\gamma_{Landau}(k_z)|(\frac{2\Delta v_z}{\pi})^{16}$ with $\gamma_{Landau}(k_z=0.35)=-0.034318\ldots$ found to be sufficient to avoid aliasing issues and completely remove the recurrence effect [36] in linear Landau damping simulations (while still recovering proper Landau damping with any desired accuracy for simulations with low-amplitude waves). Simulations with high amplitude waves (with $\Phi\sim 1$) might require higher value of hyper-viscosity coefficient D_{16v_z}, so one needs to keep track of spectrum of the solution in (z, v_z) space and adjust D_{16v_z} if needed. We typically used $D_{16v_z}=10^{-25}$ for simulations with $N_z\times N_{v_z}=64\times 256$ grid points in (z, v_z) space and $D_{16v_z}=10^{-30}$ for $N_z\times N_{v_z}=128\times 512$. Also hyper-viscosity does not affect conservation of number of particles in the system while having positive effect on conservation of energy in long-term simulations. While the term $-\frac{1}{L_z}\int_0^{L_z}f dz$ in r.h.s. side of (35) is not absolutely necessary, we found that the total energy of the system is conserved better if this term is used. This is because this term prevents filtering out of the 0th harmonic of f in z-space that holds most of the kinetic energy. Also we found that using hyper-viscosity in z direction produces similar results to the hyper-viscosity in v_z direction so only one of them is needed. We did not need any hyper-viscosity in (x, v_x) directions since the electrostatic field (and therefore both perturbations of electron density and amount of energy in high modes) in transverse direction is many orders weaker compared to longitudinal direction (z, v_z) throughout the most time of the simulation until the nonlinear self-focusing event at the end of our simulation. Detailed simulation of that event is however outside of the scope of this paper.

All simulations are carried out in the lab frame rather then in moving frame, since in this case the tails of the distribution function in v_z direction are almost symmetric and have smaller values $\propto\exp(-(v_z^{max})^2/2)$ at the boundaries $\pm v_z^{max}$ compared to the tail value $\propto\exp(-(v_z^{max}-v_\varphi)^2/2)$ in simulations done in the wave frame moving with velocity v_φ with the same v_z^{max} and the same number of grid points. For this reason simulations performed in the lab frame has smaller numerical error due to periodic BC in v_z.

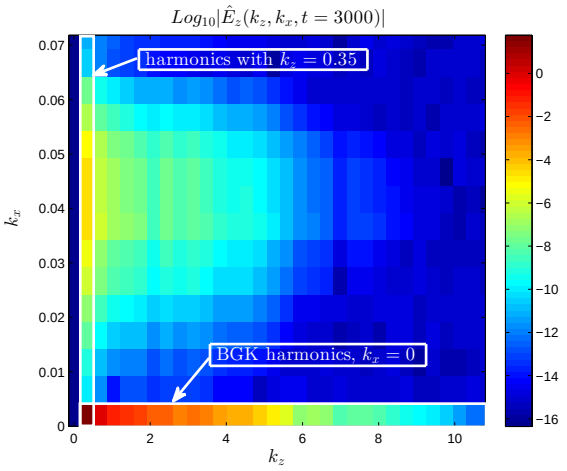

FIG. 7. The density plot of the spectrum of $E_z(z,x)$ at $t=3000$.

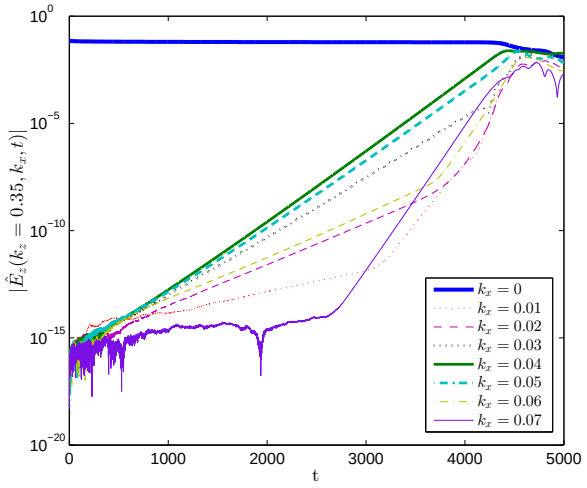

FIG. 8. The growth of harmonics $|\hat{E}_z(k_z=0.35,k_x,t)|$ in time.

B. 2+2D simulations and transverse instability of 1D BGK modes

In these simulations we use IC of the form of Eq. (7) that has the constructed BGK mode from Section III A in (z,v_z) directions, uniform in x-direction and has a Maxwellian distribution $f_0(v_x)$ in v_x direction,

$$f(z,v_z,x,v_x,t=0)=f_{BGK}(z,v_z)f_0(v_x). \qquad (36)$$

We run simulations for a long enough time to observe the growth of oblique harmonics of electric field with wave vectors $(k_z=0.35,k_x)$ (see Fig. 7 for the spectrum of E_z, the z component of the electric field) for several orders in magnitude (see Fig. 8), where k_z is the wavenumber corresponding to the BGK mode and k_x varies between $-k_x^{max}$ and $k_x^{max}=\pi/\Delta x$, $\Delta x=L_x/N_x$, where N_x is the number of grid points in x. The initial values in these harmonics are near the machine precision from the round-off errors. During the simulation they grow from values $\sim 10^{-16}$ to $\sim 10^{-1}$. The exponential growth rates γ_{k_x} for these harmonics are extracted (see Fig. 9) from the least-square fit when the amplitudes grow from $\sim 10^{-13}$ to $\sim 10^{-8}-10^{-6}$ (during these times a clear exponential growth $\propto e^{\gamma_{k_x}t}$ is observed before the nonlinear saturation effects become noticeable). Later in the simulation the nonlinear self-focusing effects come into play and LW filamentation occurs (see Figs. 10 and 11) transferring a significant part of electric field energy into the kinetic energy of particles. Figs. 7-11 are obtained from the simulation with $\phi_{eq}=0.2$.

This kind of simulations were done for a variety of BGK modes with $k_z=0.35$, amplitudes $0.025\le\phi_{eq}\le 0.77$ and the values of v_φ according to BGK dispersion relation (22) and (23) (see Section III B). Parameters typically used for simulations were $D_{16v_z}=10^{-25}$, the time step $\Delta t=0.1$, the final simulation time T_{final} in the range $2000\le T_{final}\le 30000$ (depending on

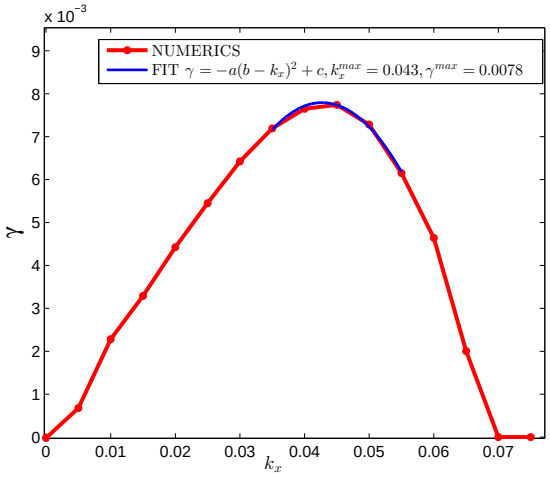

FIG. 9. The growth rates γ_{k_x} of oblique harmonics extracted from the least-square fit of the data of Fig. 8. A fit to the quadratic law near the maximum is also shown.

BGK amplitude) and $64\times256\times32\times32$ grid points for (z,v_z,x,v_x). Another set of simulations is performed for $D_{16v_z}=10^{-30}$ and $128\times512\times32\times32$ grid points with the rest of parameters being the same.

We extract the nonlinear frequency shift $\Delta\omega^{NUM}$ from simulations by finding the wave frequency as the rate of change of the phase of the Fourier harmonic of Φ with $k_z=0.35$, $k_x=0$ and subtracting frequency that corresponds to our BGK modes with zero amplitude limit, $\omega(k_z=0.35,\phi_{eq}=0)=1.2116687\ldots$, which can be obtained from Eq. (22). Note that the standard linear LW frequency (obtained using Z-function [32], see e.g. [4, 5]) is $\omega_{LW}(k_z=0.35)=1.22095\ldots$. That difference in $\sim 1\%$ is due to using of $\mathrm{Re}[\Xi_0(v_\varphi)]$ in Eq. (22) compared to $\Xi_0(v_\varphi)$ in the dispersion relation of linear LW wave. That $\sim 1\%$ difference is noticeable in $\Delta\omega$ only in the limit $\phi_{eq}\to 0$. Fig. 12 shows $\Delta\omega^{NUM}$ ob-

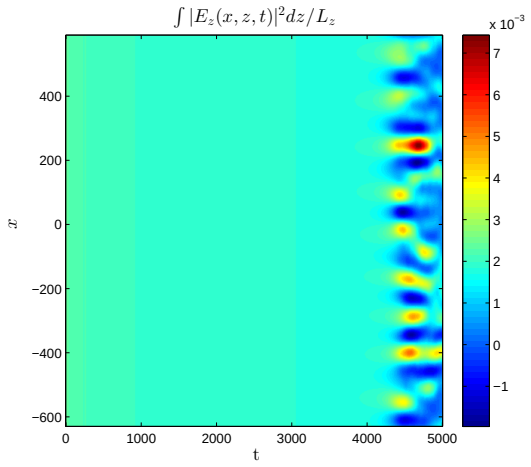

FIG. 10. The density plot vs. x and t for $\langle |E_z|^2 \rangle_z \equiv L_z^{-1} \int_0^{L_z} |E_z|^2 dz$ ($|E_z|^2$ averaged over z) shows a development of LW filamentation with time from the initial BGK mode.

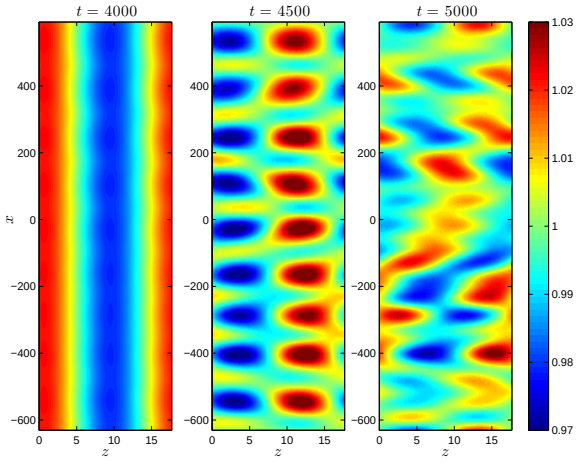

FIG. 11. Modulation of particle density $\rho(z,x)$ before ($t = 4000$), during ($t = 4500$) and after ($t = 5000$) Langmuir wave filamentation.

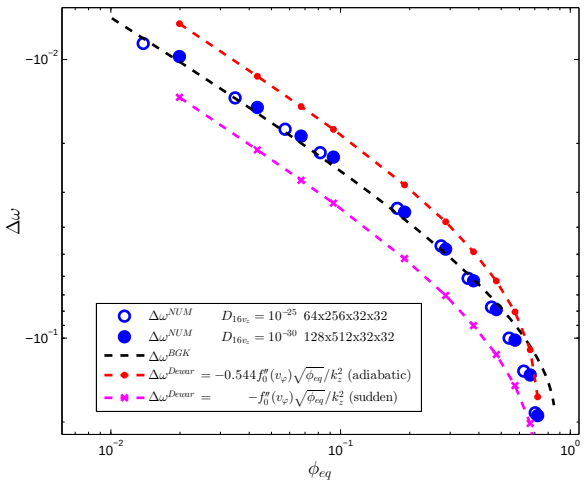

FIG. 12. Nonlinear frequency shift as a function of ϕ_{eq}.

tained from simulations in comparison with theoretical ones computed using Eq. (22) and (23) as

$$\Delta\omega^{BGK} = \omega(k_z, \phi_{eq}) - \omega(k_z, \phi_{eq} = 0). \qquad (37)$$

Another two lines of Fig. 12 show Dewar's [7] nonlinear frequency shift approximation for large-amplitude EPWs in case of sudden and adiabatic pumping given by

$$\Delta\omega_{NL}^{Dewar} = -\alpha f_0''(v_\varphi)\sqrt{\phi_{eq}}/k_z^2, \qquad (38)$$

where $\alpha = 0.544$ and $\alpha = 1$ for the adiabatic pumping and the sudden pumping of nonlinear LW, respectively.

We conclude from Fig. 12 that $\Delta\omega^{BGK}$ (37) works really well for amplitudes of BGK $\phi_{eq} \lesssim 0.5$. Also $\Delta\omega^{NUM}$ is located within bounds from two Dewar's solutions for the whole range of amplitudes.

Growth rates of transverse instability from the series of simulations with $D_{16v_z} = 10^{-30}$ and $128 \times 512 \times 32 \times 32$ grid points for (z, v_z, x, v_x) and various amplitudes ϕ_{eq} are given in Figs. 13 and 14. The maximum growth rate γ^{max} (the maximum vs. k_x for each fixed ϕ_{eq}) as a function of ϕ_{eq} is shown in Fig. 15 (for two numerical grids, filled and non-filled circles, respectively) together with the theoretical predictions given by Eqs. (22), (23), (25) and (27) (dashed-dotted line of sand color) and given by Eqs. (25) and (28) (dashed-dotted line of brown color). Other lines in Fig. 15 use the leading order approximation in ϕ_{eq} given by Eq. (32) with four estimates for $\Delta\omega$: (a) from simulations $\Delta\omega = \Delta\omega^{NUM}$; (b) from Eq. (37), $\Delta\omega = \Delta\omega^{BGK}$ and (c),(d) $\Delta\omega = \Delta\omega_{NL}^{Dewar}$ from two cases of Eq. (38).

We conclude from Fig. 15 that while theoretical prediction based on Eqs. (22), (23), (25) and (27) claims no growth for the amplitudes $\phi_{eq} \gtrsim 0.3$, we still observe the growth for even higher amplitudes. Eqs. (25) and (28) predict growth for any amplitudes but differ from the numerical results by $\sim 70\%$ while approximations $\gamma^{max} \approx |\Delta\omega^{BGK}|/4$ and $\gamma^{max} \approx |\Delta\omega^{NUM}|/4$ work better (especially for amplitudes $\phi_{eq} > 0.1$) staying almost identical to each other for amplitudes of BGK $\phi_{eq} \lesssim 0.5$. In all these comparisons with theory we assumed in Eq. (25) that $\nu_{residual} = 0$ consistent with the expected absence of sideloss in the periodic BC in x as discussed in the beginning of Section IV. We also tried the empirical suggestion of Ref. [23] to include the amplitude-dependent anisotropic Landau damping into $\nu_{residual}$ but found that such term makes the agreement between the theory and simulations worse.

The wavenumber $k_x = k_x^{max}$ at which the growth rate has the maximum is shown in Fig. 16 as a function of ϕ_{eq} together with the theoretical predictions. The same style of lines of Fig. 16 as in Fig. 15 correspond to the same approximations. Dashed-dotted line of sand color represents prediction by Eqs. (22), (23), (25) and (27), dashed-dotted line of brown color represents prediction by Eqs. (25) and (28), other lines in Fig. 16 use the leading order approximation in ϕ_{eq} given by Eq. (34) with the BGK mode group velocity v_g defined in Eq. (28). They include different estimates of $\Delta\omega$, from Dewar's

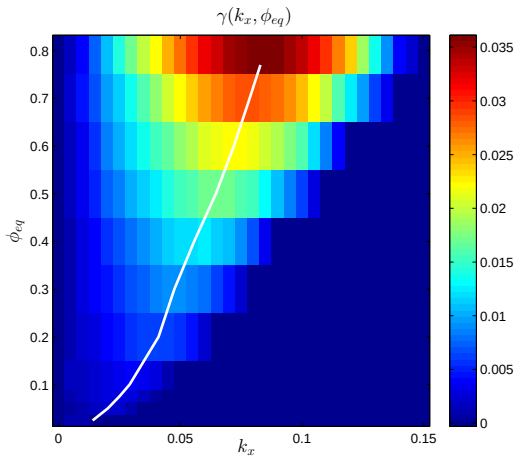

FIG. 13. The density plot of the growth rate γ_{k_x} as a function of k_x and BGK amplitude ϕ_{eq}. The white line shows the position of the maximum γ_{k_x} over k_x for each ϕ_{eq}.

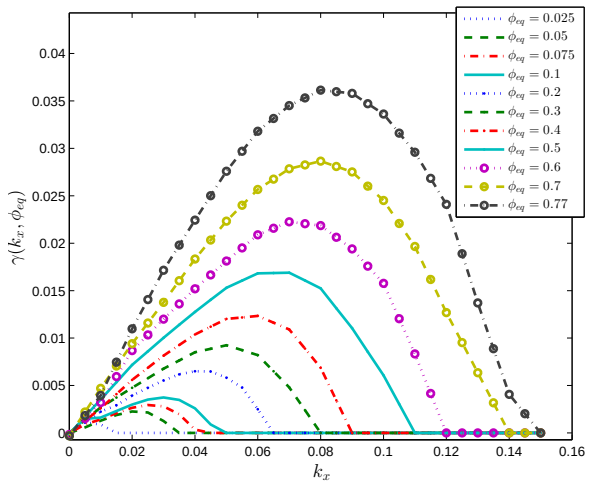

FIG. 14. The growth rates γ_{k_x} as a function of k_x for BGK modes with various amplitudes ϕ_{eq} correspond to multiple cross-sections of Fig. 13.

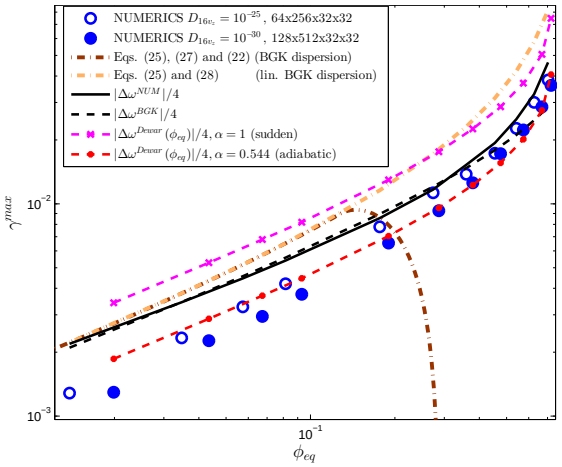

FIG. 15. The maximum growth rate as a function of ϕ_{eq}.

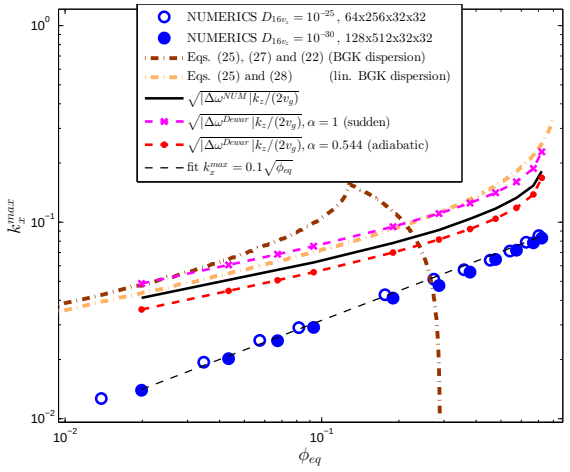
NUMERICS $D_{16v_z} = 10^{-25}$, 64x256x32x32
NUMERICS $D_{16v_z} = 10^{-30}$, 128x512x32x32
Eqs. (25), (27) and (22) (BGK dispersion)
Eqs. (25) and (28) (lin. BGK dispersion)
$\sqrt{|\Delta\omega^{NUM}|k_z/(2v_g)}$
$\sqrt{|\Delta\omega^{Dewar}|k_z/(2v_g)}, \alpha = 1$ (sudden)
$\sqrt{|\Delta\omega^{Dewar}|k_z/(2v_g)}, \alpha = 0.544$ (adiabatic)
fit $k_x^{max} = 0.1\sqrt{\phi_{eq}}$
k_x^{max}
ϕ_{eq}

FIG. 16. The wavenumber k_x^{max} at which the growth rate reaches the maximum as a function of ϕ_{eq}.

model (38) and measured $\Delta\omega^{NUM}$. All theoretical approximations predict $k_x^{max} \propto \phi_{eq}^{1/4}$ for small amplitudes but failed to agree with numerical results for k_x^{max} somewhat well as seen in Fig. 16. It is also seen in Fig. 16 from the thin dashed line that the empirical dependence $k_x^{max} \sim 0.1\sqrt{\phi_{eq}}$ fits the numerical results pretty well but remains to be explained theoretically.

We also investigated the convergence of growth rates with $D_{16v_z} \to 0$ while $\Delta z, \Delta v_z \to 0$ and, correspondingly, $N_z, N_{v_z} \to \infty$ while keeping $N_x = 32, N_{v_x} = 32$ (the discretization in x space does not affect the error in growth rates and 32 points is enough to resolve the Maxwellian distribution in v_x direction with spectral precision). We found that the relative errors in our numerical results for growth rates with $D_{16v_z} = 10^{-30}$ and 128x512x32x32 grid points for (z, v_z, x, v_x) are within $10 - 15\%$ range.

C. Comparison of transverse instability growth rates with PIC code simulations

We now compare γ_{k_x} that we obtained in Section IV B from our simulations for the mode with $(k_z = 0.35, k_x = 0.05)$ to the growth rates of the same mode obtained using PIC simulations in Fig. 9(j) of Ref. [20] for three different amplitudes of BGK modes: $\phi_{eq} = 0.2, 0.3, 0.5$. These BGK modes in both cases were constructed using $k_z = 0.35$ and have $v_\varphi = 3.35818,\ 3.32288,\ 3.23266$, respectively. Our growth rates for these three amplitudes are 0.0073, 0.0113 and 0.0158. The corresponding growth rates from Ref. [20] are 0.0075, 0.012, and 0.0147, i.e. only $\sim 10\%$ difference with our results.

The total number of particles used in Ref. [20] was $\approx 2 \times 10^8$ with 32x1280 cells and 5000 particles per cell. Number of grid points in our simulations was 64x256x32x32 for (z, v_z, x, v_x) (total $\approx 1.6 \times 10^7$) with $L_z = 2\pi/k_z, L_x = 200\pi, v_z^{max} = 8, v_z^{max} = 6$, and $D_{16v_z} = 10^{-25}, \Delta t = 0.1, T_{final} = 5000$.

V. CONCLUSION

We studied the filamentation of Langmuir wave in the kinetic regime $k\lambda_D \gtrsim 0.2$ considering the transverse instability of the particular family of BGK modes that is a bifurcation of the linear Langmuir wave and approximates the nonlinear electron plasma wave resulting from the adiabatically slow pumping by SRS. The construction process of these BGK modes is described in detail. Performing direct $2+2D$ Vlasov-Poisson simulations of collisionless plasma we found that the maximal growth rates from simulations are $50-70\%$ smaller compered to the theoretical prediction but exhibit the proper scaling for small amplitudes of BGK wave $\gamma^{max} \propto \sqrt{\phi_{eq}}$ while $k_x^{max} \propto \sqrt{\phi_{eq}}$ result remains to be explained theoretically since current theory predicts $k_x^{max} \propto (\phi_{eq})^{1/4}$.

ACKNOWLEDGMENTS

This work was supported by the National Science Foundation under Grants No. PHY 1004118, No. PHY 1004110 and DMS-1412140. Simulations were performed at the Texas Advanced Computing Center which was supported by National Science Foundation Grant ACI-1053575.

[1] H. A. Rose and D. A. Russell, Physics of Plasmas **8**, 4784 (2001).
[2] I. B. Bernstein, J. M. Greene, and M. D. Kruskal, Phys. Rev. **108**, 546 (1957).
[3] N. A. Krall and A. W. Trivelpiece, *Principles of Plasma Physics* (McGraw-Hill Inc., New York, 1973).
[4] E. M. Lifshitz and L. Pitaevskii, *Physical Kinetics: Volume 10* (Butterworth-Heinemann, Oxford, 1981).
[5] D. R. Nicholson, *Introduction to Plasma Theory*, Vol. XII (John Wiley & Sons, New York, 1983).
[6] W. M. Manheimer and R. W. Flynn, Physics of Fluids **14**, 2393 (1971).
[7] R. L. Dewar, Physics of Fluids **15**, 712 (1972).
[8] G. J. Morales and T. M. O'Neil, Phys. Rev. Lett. **28**, 417 (1972).
[9] H. A. Rose, Physics of Plasmas **12**, 012318 (2005), http://dx.doi.org/10.1063/1.1829066.
[10] K. J. Bowers, B. J. Albright, L. Yin, B. Bergen, and T. J. T. Kwan, Physics of Plasmas **15**, 055703 (2008), http://dx.doi.org/10.1063/1.2840133.
[11] L. Yin, B. J. Albright, H. A. Rose, K. J. Bowers, B. Bergen, D. S. Montgomery, J. L. Kline, and J. C. Fernandez, Physics of Plasmas **16**, 113101 (2009), http://dx.doi.org/10.1063/1.3250928.
[12] M. V. Goldman and D. F. Du Bois, Physics of Fluids **8**, 1404 (1965).
[13] D. A. Russell, D. F. DuBois, and H. A. Rose, Physics of Plasmas **6**, 1294 (1999).
[14] D. S. Montgomery, J. A. Cobble, J. C. Fernandez, R. J. Focia, R. P. Johnson, N. Renard-LeGalloudec, H. A. Rose, and D. A. Russell, Physics of Plasmas **9**, 2311 (2002).
[15] J. L. Kline, D. S. Montgomery, B. Bezzerides, J. A. Cobble, D. F. DuBois, R. P. Johnson, H. A. Rose, L. Yin, and H. X. Vu, Phys. Rev. Lett. **94**, 175003 (2005).
[16] C. E. Max, J. Arons, and A. B. Langdon, Phys. Rev. Lett. **33**, 209 (1974).
[17] A. J. Schmitt and B. B. Afeyan, Physics of Plasmas **5**, 503 (1998).
[18] P. M. Lushnikov and H. A. Rose, Plasma Physics and Controlled Fusion **48**, 1501 (2006).
[19] P. M. Lushnikov and H. A. Rose, Phys. Rev. Lett. **92**, 255003 (2004).
[20] L. Yin, B. J. Albright, K. J. Bowers, W. Daughton, and H. A. Rose, Physics of Plasmas **15**, 013109 (2008), http://dx.doi.org/10.1063/1.2825663.
[21] H. A. Rose and L. Yin, Physics of Plasmas **15**, 042311 (2008), http://dx.doi.org/10.1063/1.2901197.
[22] H. A. Rose and W. Daughton, Physics of Plasmas **18**, 122109 (2011), http://dx.doi.org/10.1063/1.3662112.
[23] R. L. Berger, S. Brunner, J. W. Banks, B. I. Cohen, and B. J. Winjum, Physics of Plasmas **22**, 055703 (2015), http://dx.doi.org/10.1063/1.4917482.
[24] Y. Kato, K. Mima, N. Miyanaga, S. Arinaga, Y. Kitagawa, M. Nakatsuka, and C. Yamanaka, Phys. Rev. Lett. **53**, 1057 (1984).
[25] J. D. Lindl, P. Amendt, R. L. Berger, S. H. G. S. G. Glendinning, S. W. Haan, R. L. K. O. L. Landen, and L. J. Suter, Phys. Plasmas **11**, 339 (2004).
[26] N. B. Meezan, L. J. Atherton, D. A. Callahan, E. L. Dewald, S. Dixit, E. G. Dzenitis, M. J. Edwards, C. A. Haynam, D. E. Hinkel, O. S. Jones, O. Landen, R. A. London, P. A. Michel, J. D. Moody, J. L. Milovich, M. B. Schneider, C. A. Thomas, R. P. J. Town, A. L. Warrick, S. V. Weber, K. Widmann, S. H. Glenzer, L. J. Suter, B. J. MacGowan, J. L. Kline, G. A. Kyrala, and A. Nikroo, Phys. Plasmas **17**, 056304 (2010).
[27] J. P. Holloway and J. J. Dorning, Phys. Rev. A **44**, 3856 (1991).
[28] M. Buchanan and J. Dorning, Phys. Rev. E **52**, 3015 (1995).
[29] T. O'Neil, Physics of Fluids **8**, 2255 (1965).
[30] A. A. Vlasov, Soviet Physics Uspekhi **10**, 721 (1968).
[31] L. D. Landau, J. Phys.(USSR) **10**, 25 (1946), [Zh. Eksp. Teor. Fiz.16,574(1946)].
[32] B. D. Fried, M. Gell-Mann, J. D. Jackson, and H. W. Wyld, Journal of Nuclear Energy. Part C, Plasma Physics, Accelerators, Thermonuclear Research **1**, 190 (1960).
[33] D. S. Montgomery, R. J. Focia, H. A. Rose, D. A. Russell, J. A. Cobble, J. C. Fernández, and R. P. Johnson, Phys. Rev. Lett. **87**, 155001 (2001).
[34] W. L. Kruer, J. M. Dawson, and R. N. Sudan, Phys. Rev. Lett. **23**, 838 (1969).
[35] P. M. Lushnikov, H. A. Rose, D. A. Silantyev, and N. Vladimirova, Phys. of Plasmas **21**, 072103 (2014).
[36] C. Cheng and G. Knorr, J. of Comp. Phys. **22**, 330 (1976).